Investigation of soot oxidation by coupling LII, SAXS and scattering measurements

Jérôme Yon, François-Xavier Ouf, Damien Hébert, James Brian Alexander Mitchell, Nadine Teuscher, Jean-Luc Le Garrec, Alexandre Bescond, Werner Baumann, Djoudi Ourdani, Thomas Bizien, et al.

INVESTIGATION OF THE SOOT OXIDATION BY COUPLING LII, SAXS AND SCATTERING MEASUREMENTS

Jérôme Yon[1], François-Xavier Ouf[2], Damien Hebert[1], James Brian Mitchell[3], Nadine Teuscher[4], Jean-Luc Le Garrec[3], Alexandre Bescond[5], Werner Baumann[4], Djoudi Ourdani[6], Thomas Bizien[7] and Javier Perez[7].

[1] Normandie Univ, INSA Rouen, UNIROUEN, CNRS, CORIA, 76000 Rouen, France.

[2] Institut de Radioprotection et de Sureté Nucléaire (IRSN), PSN-RES, SCA, LPMA, Gif-sur-Yvette, 91192, France.

[3] Institut de Physique de Rennes, Université de Rennes I, 35042 Rennes, France.

[4] Institute for Technical Chemistry, Karlsruhe Institute of Technology, Germany.

[5] Environnement SA, 78304 POISSY, France

[6] Laboratoire de Physico-Chimie des Matériaux et Catalyse, Université de Bejaia, 06000 Bejaia, Algérie.

[7] Synchrotron SOLEIL, L'orme des Merisiers Saint-Aubin – BP 48, Gif-sur-Yvette, 91192, France.

KEYWORDS

Soot, oxidation, laser, SAXS, fractals

CORRESPONDING AUTHOR

Dr Jérôme YON yon@coria.fr

ABSTRACT

This work presents an *in-situ* characterization of the soot oxidation phenomenon in flames by coupling three different techniques. Small Angle X-ray Scattering and Static Light Scattering were used in order to provide information on the size of the primary spheres and the aggregates respectively. Laser Induced Incandescence was also used to determine the soot volume fraction in the flame. Furthermore, flame temperatures and soot residence time were also determined. These techniques were combined for a precise description of the impact of the oxidation process on the soot aggregates (aggregate and primary sphere densities, size distributions). In order to limit the phenomena to oxidation, soot was generated upstream by a miniCAST generator and injected in a non-sooting flame. Amongst other results, it is shown that primary sphere diameter reduction is accompanied by an increase of the geometric standard deviation suggesting that the mass loss rate on the scale of the primary spheres, is size dependent, certainly caused by the local action of the oxidation mechanisms in the vicinity of the particle surface.

INTRODUCTION

Soot oxidation is a key phenomenon enabling the quantity of nanoparticles produced during the combustion process (automobile emissions, aircraft and marine ship engine emissions) to be reduced. The literature is well documented on this topic, the reader is invited to refer to the review article by Stanmore et al. (2001). Nevertheless, most of these studies are *ex-situ*, relying on gravimetric measurements of samples deposited in furnaces. If these investigations are of interest for the optimization of different catalytic processes including the regeneration of particulate filters, they do not allow the physical processes involved in the oxidation of soot particles, to be completely

understood. However, the reduction of the soot particle emissions from different combustion systems can also be envisaged by an optimization of the combustion process itself. Numerical modeling is a promising tool to reach this goal; nevertheless, the main mechanisms involved in the soot formation (mainly surface growth and oxidation) need to be better understood (Mueller et al. 2011). To reach this goal, many studies have been performed in flames for soot characterization under the oxidation process by ex-situ techniques (Ghiassi et al. 2016; Jung et al. 2004; Kim et al. 2005; Lee et al. 1962; Lighty et al. 2011; Ma et al. 2013; Puri et al. 1994) or in-situ optical techniques (Garo et al. 1988; Garo et al. 1990; Neoh et al. 1985; Xu et al. 2003), the latter generally based on laser light extinction, scattering and the depolarization ratio. Most of these studies, however, cannot isolate oxidation from surface growth mechanisms occurring within sooting flames. One interesting way to overcome this drawback and to focus on the oxidation process is to inject previously produced soot particles into a non-sooting flame (I.e. a "*two stage burner*") as previously done by Neoh et al. (1985), Lighty et al. (2011), Echavarria et al. (2011) and very recently by Ghiassi et al. (2016) and Sirignano et al. (2016). Except for Neoh et al., however, all this work was *ex-situ* involving a sampling of the particles. Neoh et al. (1985) performed optical and *in-situ* measurements on a two-stage burner by coupling light scattering and extinction but their results were based on Mie theory, thus considering soot as spherical particles. Unfortunately, it was shown that Mie theory was not relevant for fractal aggregates (Dobbins and Megaridis 1991). Moreover, use of visible light does not allow the very small scales, typical of those of the primary spheres (around 30 nm) to be investigated. Small Angle X-ray Scattering (SAXS) is a very powerful technique that enables the size and shape at the smallest scales of nanoparticles to be characterized. This technique has been already used for the *in-situ* characterization of soot (Di Stasio et al. 2011; Di Stasio et al. 2006; Mitchell et al. 2013; Mitchell et al. 2006; Ossler et al. 2013) but these studies were not focused on the specific study of the oxidation process. Nevertheless, most of the SAXS experiments do not allow information concerning primary particle diameter and aggregate size to be obtained at the same time, when one exceeds 100 nm. It is the reason why complementary measurements based on visible Static Light Scattering (SLS) are still important. Finally, one of the most powerful optical and *in-situ* techniques for characterizing the local soot volume fraction in flames, is Laser Induced Incandescence (LII) (Michelsen et al. 2015). For all these reasons, this work

aims to combine SAXS, SLS and LII for the characterization of soot particles under oxidation by using a two-stage burner. The main improvement in comparison to the work by Neoh et al. (1985) is the coupling of three complementary techniques and the use of an optical model, dedicated to fractal aggregates. This coupling enables the primary particle size distribution, number density, aggregate size, soot volume fraction and surface area to be determined. The impact of oxidation on the primary sphere internal microstructure cannot be investigated by these techniques; nevertheless, this aspect has already been examined in previous studies (Ishiguro et al. 1991; Ishiguro et al. 1997; Schmid et al. 2011; Seong and Boehman 2012).

In the following, the experimental setup will be presented followed by the raw results in section 3. The analysis section will present the methodology for the extraction of the different physical parameters and the last section will present the results and their analysis.

EXPERIMENTAL APPARATUS

The experiment is shown in FIG. 1. First, soot is produced by a miniCAST burner. A thermodenuder (TSI 3065) is used to ensure that volatile species are removed from the particles. A bypass permits to deliver soot and its surrounding gas at the center of the McKenna burner or only the surrounding gas by using a high-efficiency filter (MSA Safety). This was used for the subtraction of the background signal for SAXS measurements. Once injected in the non-sooting flame (described hereafter) the soot temperature increases and produces the thermal emission (yellow part of the flame shown on the picture in Fig. 1-A) and the oxidation of soot particles. The burner was positioned on a 3D movable table allowing the SAXS signal to be measured for different heights above the burner (HAB). In addition to the SAXS experiment, a Nd:YAG laser was used for the LII and SLS measurements (Fig. 1-B), described in a forthcoming subsection.

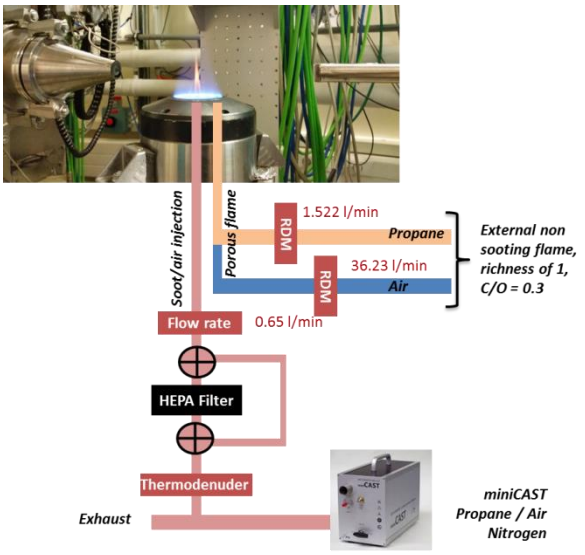

A: Injection of soot produced by miniCAST at the center of the non-sooting flame (modified McKenna Burner). The picture represents the SAXS experiment at SOLEIL (Swing beamline).

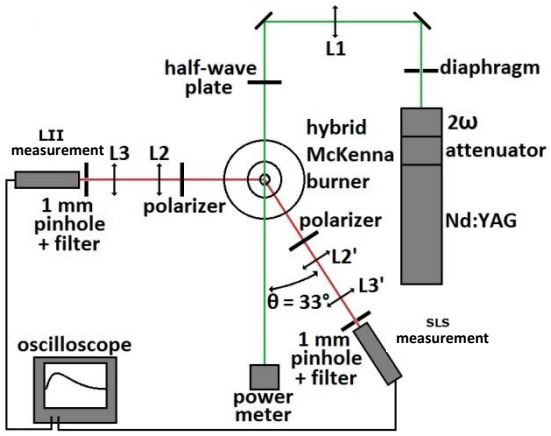

B: Experimental apparatus for the LII and SLS experiments (seen from above).

FIG. 1 Experimental setup

SOOT GENERATION AND ITS CHARACTERIZATION

A commercial miniCAST generator (model 5206, Jing Ltd.) was used to generate soot particles under stable and repeatable operating conditions. For more information concerning the characterization of the soot produced by the miniCAST and the operation of this burner, please refer to (Moore et al. 2014). The selected operating condition was in accordance with (Bescond et al. 2016; Yon et al. 2015) but the dilution air was turned off in order to increase the particle concentration for the SAXS experiments. The corresponding characteristics of the generated particles are reported in Table 1 (note that values marked with a superscript asterisk in Table 1 were extracted from (Bescond et al. 2016; Yon et al. 2015) based on the assumption that these parameters are unaffected by the dilution air; all other values were determined in the present study). The size distribution of the generated soot particles was determined using a Scanning Mobility Particle Sizer (SMPS) (TSI). It was found to be lognormal, the corresponding modal diameter, geometric standard deviation and number concentration being reported in Table 1. Note that reported values were corrected with a dilution of (1:100) produced by a PALAS VKL dilution system, in order to avoid the saturation of the SMPS. A model for the conversion of the size distribution based on mobility diameter to the size distribution based on

gyration diameter, based on (Yon et al. 2015), was applied. The corresponding modal diameter and geometric standard deviation are marked in Table 1 with indices **. In addition, the volume fraction of the generated particles was determined using a Pegasor Particle Sensor (PPS), initially calibrated for the miniCAST operating condition using a TEOM (R&P 1105) ambient particulate monitor. Finally, the organic content (OC/TC ratio) was determined using a SUNSET LAB thermoanalyzer with the IMPROVE_A protocol.

SMALL ANGLE X-RAY SCATTERING

The SAXS experiments were performed on the SWING beamline at the SOLEIL synchrotron in France during June 2015. A 12 keV (1 Å) collimated, monochromatic X-ray beam was used and the distance between the detector and the flame was fixed to 1.7 m corresponding to spectral analysis in the domain $0.006 < q < 0.05\ (\text{Å}^{-1})$, where q=(4π/λ)sin(θ/2), with λ and θ being the wavelength of the incident radiation and the scattering angle, in order to have a good characterization of the scale of the soot primary particles size assuming a diameter D~π/λ, this range corresponds to particles of between about 6 and 50 nm.

TAB 1. Operating conditions and properties of particles produced with the miniCAST

CAST operating conditions	Propane (mL/min)	60
	Nitrogen (mL/min)	0
	Oxidation air (L/min)	1.5
	Dilution air (L/min)	0
TEM	Primary sphere modal diameter (nm) *	26.6
	Standard deviation of the log-normal primary sphere diameter size distribution (nm) *	1.31
	Fractal dimension (-)*	1.73
	Fractal prefactor (-)*	1.94
SMPS	Modal mobility diameter (nm)	157
	Modal gyration diameter (nm) **	222
	Geometric mobility standard deviation (-)	1.57
	Geometric gyration standard deviation (-)**	1.9
	Number concentration ($\times 10^{13}$ part./m^3)	3.65
Effective density	Density (kg/m^3) *	1543
PPS	Volume fraction (ppb)	27.2
Thermoanalysis	OC/TC (%) (±5%)	4.1*
	OC/EC (%) (based on OC/TC)	4.3

LASER INDUCED INCANDESCENCE (LII) AND STATIC LIGHT SCATTERING (SLS)

A Q-switched Nd:YAG (Quantel Brilliant EaZy) with a pulse width of 5 ns FWHM operated at 10 Hz was used. Laser fluence was controlled with a beam attenuator module coupled with a power meter (Gentec Maestro). A half-wave plate was used to obtain a fixed vertical polarization state (orthogonal to the scattering plane) for all the experiments. Two excitation wavelengths were available depending

on the type of measurement. For LII measurements, the first harmonic (1064 nm) was used as the exciting wavelength. For SLS measurements, the second harmonic (532 nm) was generated using a doubler module (2ω). To obtain a beam with a more uniform energy distribution, a rectangular profile was generated using a 1-mm diaphragm coupled with a lens with a focal length of 35 cm (L1 in Fig. 1-B). A beam analyzer (Photon USBeamPro CCD) was used to ensure similar laser beam profiles for both excitation wavelengths; this correspondence was accomplished by adjusting the position of the L1 lens (profiles not presented). The laser beam had a diameter of 1.8 mm at the center location of the hybrid McKenna burner. For both excitation wavelengths, the laser fluence was set at 0.2 J/cm², preventing the occurrence of any sublimation.

Signals were collected using two identical optical paths (Fig. 1-B) consisting of a polarizer (in vertical position), two lenses (focal lengths of L2 = L2' = 20 cm and L3 = L3' = 10 cm), a 1-mm pinhole, a bandpass filter (λ_{de} = 532 nm for SLS and 442 nm for LII at 10 nm FWHM), and a photomultiplier (PM, Hamamatsu H3378-50). The first arm was positioned at 90° for LII measurements and at 33° for the SLS measurements. An oscilloscope (LeCroy WavePro 725Zi 2.5 GHz) was used for signal acquisition. Each measurement represented an average of 200 measurements, thereby allowing uncertainties to be evaluated.

THE OXIDIZING FLAME

The non-sooting flame was generated by a hybrid McKenna burner (Fig. 1-A). The premixed air/propane flame was attached to a porous bronze plate with a diameter of 60 mm at a flow rate of 36.23 L/min for air and of 1.522 L/min for propane corresponding to a stoichiometric flame. The flame was stabilized with an external air-flow ring. The aerosol was injected into the center tube (6 mm diameter) of the burner at a flow rate of 0.63 L/min (measured with a Gilibrator-2 Calibration System from Sensidyne). The temperature of the porous plate was regulated by oil circulation maintained at 16 °C.

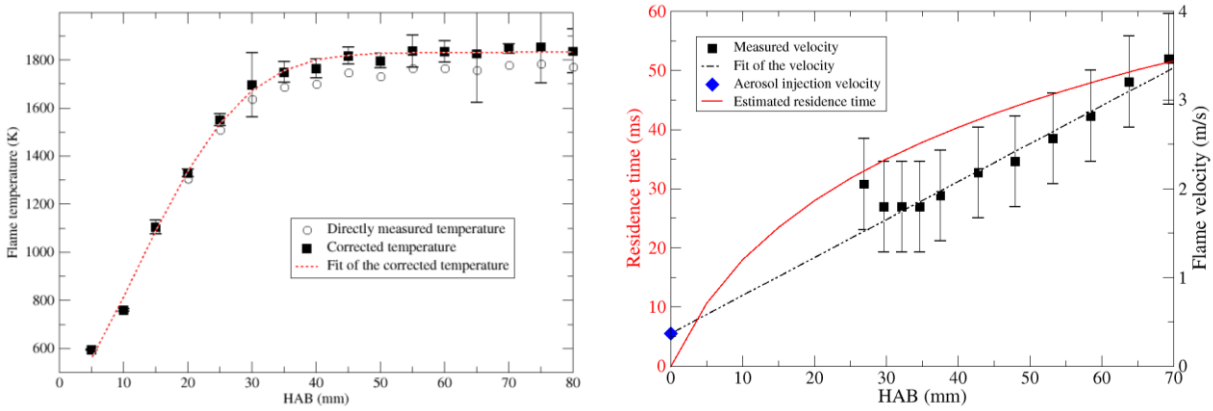

A: Temperature profile B: Residence time

FIG. 2 Determination of the non-sooting flame temperature and residence time as a function of the height above the burner (HAB).

The vertical temperature profile (Fig. 2-A) of the flame was determined by inserting a thermocouple type B at different heights above the burner. Note that measurements were performed without soot injection into the non-sooting flame. Hence, the measurements were not affected by the soot deposition on the thermocouple and by the radiation of these particles. Nevertheless, the radiation of the thermocouple had to be taken into account by determining the convective heat transfer and the emissivity of the thermocouple based expressions respectively and the formulae reported in (Bradley and Matthews 1968) and (Lyons and Gracia-Salcedo 1989). The expression of the fitted curve (dash red line in Fig. 2-A) is given in Equation 1.

$T = 915 \times \left(1 + erf\left(\frac{z \times 100 - 1.18}{1.88}\right)\right)$ with z the HAB expressed in m and T in K. [1]

The residence time in the flame was determined using particle vaporization velocimetry (Seitzman et al. 1999). This technique consists in using high fluence in order to instantaneously sublimate the soot particles. The so produced “hole” in the flame is shifted in time at the local velocity of the flame. This velocity is then determined by imaging the flame with an intensified camera with and without applying a temporal offset (2 ms). For this experiment, in order to enhance the detection, the central injection of miniCAST aerosol flow-rate was reduced to 0.6 L/min and enriched with 30 mL/min of propane in order to enhance the generation of soot at the center of the burner. The obtained velocities are reported in Figure 2-B (black filled squares). Unfortunately, the natural emission of soot was too

low at the bottom of the flame (i.e. for HAB lower than 30 mm) and the technique was no longer practical at these low HAB distances. The observed linear tendency of the flame velocity versus HAB was then extrapolated up to HAB = 0 mm (black dashed curve in Fig. 2-B) showing good agreement with the aerosol injection velocity at the center of the McKenna burner (blue diamond). The integration of this linear tendency allows the residence time (red plain curve) to be evaluated, corresponding to the Eq. 2:

$t_{res} = \frac{1}{a}\ln\left(\frac{a}{b}z + 1\right)$ based on $v = ax + b$ with $a = 42.76\ s^{-1}$, $b = 0.37\ m.s^{-1}$, z the HAB expressed in m and t_{res} in s. [2]

The values obtained are comparable with values measured by Xu et al. (1997) in a premixed ethylene/air flame with a McKenna burner as well as values computed by Kong et al. (2009) for a methane/air flame.

RESULTS

In Figure 3-A we present the results obtained with the SAXS experiment. As expected, the signal decreased with the height above the burner suggesting a decrease of soot mass concentration within the flame due to the oxidation process. In this representation of the data, however, there is no clear evidence of a decrease of the particle size nor of a change of surface roughness. Figure 3-B represents the same results by means of a Porod plot *i.e.* the signal is multiplied by q^4 and plotted vs q. Indeed, for smooth spheres, with a sharp interface with the surrounding medium, the signal intensity will decrease as q^{-4} at large q and so, in this case, the Porod plot will present a plateau, parallel to the abscissa. This plateau is well observed indicating that primary spheres keep presenting a smooth interface during the oxidation process, contrarily to oxidation of metallic nanoparticles, studied in a recent experiment (Förster et al. 2015) that presented a more rugged surface in the presence of a high oxygen concentration atmosphere. Moreover, we also observed a progressive shift of the plateau to the larger q parameter as the HAB increased. This is a first qualitative indication that primary particle size decreases during the oxidation process.

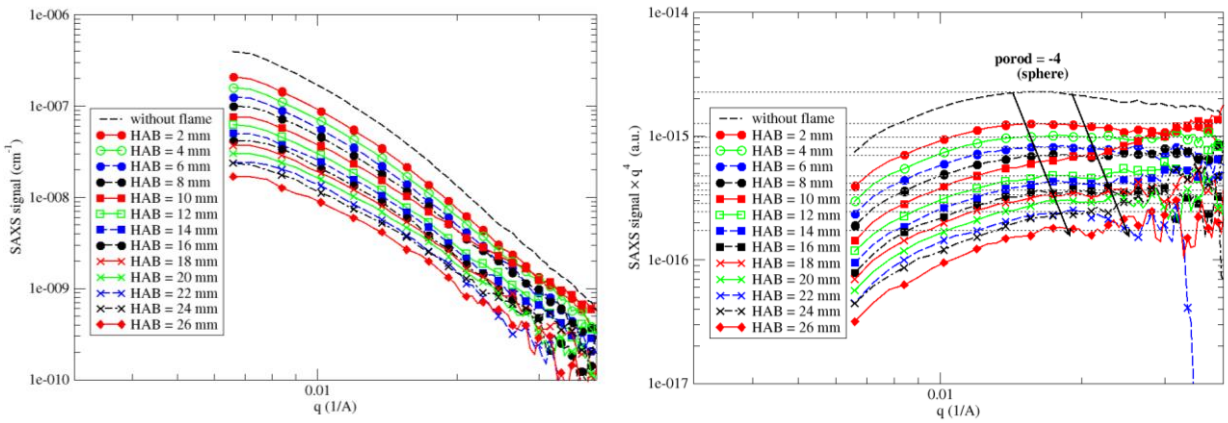

A: Conventional plot B: Porod plot

FIG. 3 Results of the SAXS signals as a function of the height above the burner.

The maximum of the LII signal as a function of the HAB is shown as solid black circles in the upper panel of Figure 4. As with the SAXS measurements, this signal is seen to decrease with HAB suggesting a decrease of the soot volume fraction. Nevertheless, even if the LII signal is often considered to be proportional to the volume fraction, as will be explained further in the analysis section, a significant change of the local temperature as well as a change of soot primary particle, may also influence the LII signal. We will show that taking these effects into account yields the red curve in the upper panel of FIG. 4.

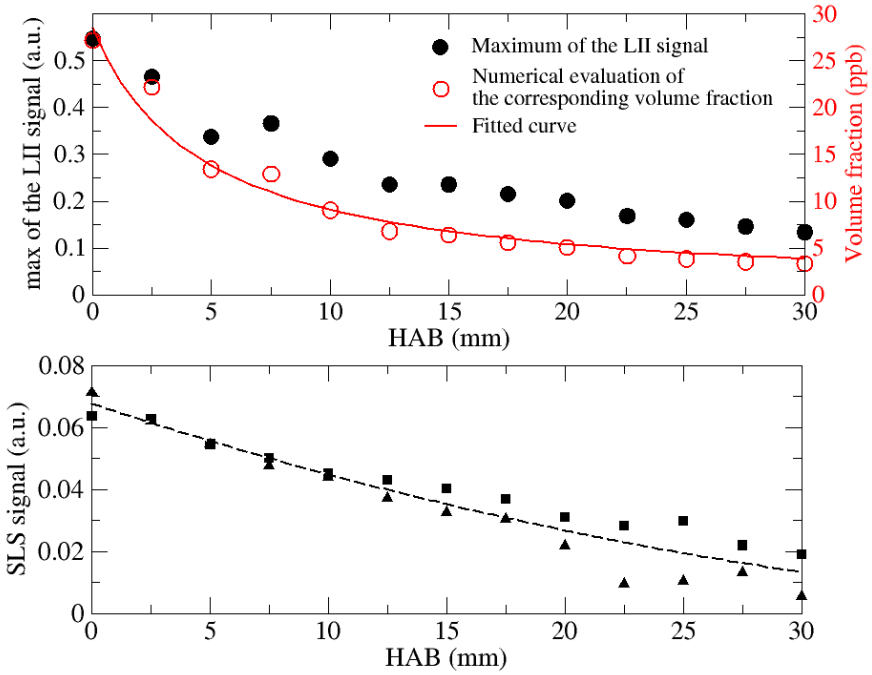

FIG. 4 Results of the LII (upper panel) and SLS measurements (lower panel).

Two consecutive measurements of the scattering signal, collected at 33° scattering angle, are shown in the lower panel of FIG. 4. These two measurements highlight the uncertainty of the results at HABs larger than 20 mm. In the remainder of the document, the fitted (black dashed curve) will be considered.

ANALYSIS

In this section, we present the methodology used for the interpretation of the results presented in the previous section in terms of the evolution of soot volume fraction, primary particle size, aggregate size and number density during the oxidation process.

MODELING OF THE SCATTERING DATA (SAXS AND SLS)

When photons elastically interact with matter, most are forward scattered but some of them are scattered into other angles. When a flux of photons is collected at a given scattering angle θ, its intensity is affected due to the interferences occurring by summing electromagnetic radiations coming from different locations of the particles, leading to different optical path differences. Consequently, the angular dependence of the scattered intensity is a marker of the particle size and shape. Whether for SAXS or SLS, the phenomena are similar and it is generally preferred to interpret the signals as a

function of the magnitude of the scattering wave vector $q = \frac{4\pi}{\lambda} sin\left(\frac{\theta}{2}\right)$ instead of using the scattering angle θ. The inverse of q is an order of magnitude of the technique sensitivity to the particle size (Sorensen 2013). It is clear therefore that SLS and SAXS, based respectively on visible and X-ray photons, will probe soot particles at different and complementary size scales. More precisely, hard x-ray SAXS is typically used for particles whose size is between a few nm to a hundred nm whereas SLS will cover sizes between 50 and 500 nm. Consequently, for soot particles, the former technique will be of particular interest for the description of the primary spheres whereas the latter will be adapted for the description of the aggregate size. When the signals are integrated over a large population of isotropically oriented particles, the scattering pattern is generally smooth and can be interpreted by asymptotic theories. For soot particles, SLS angular measurements are generally interpreted with the help of the Rayleigh Debye-Gans Theory for Fractal Aggregates (RDG-FA) introduced by Dobbins and Megaridis (1991) and used by many researchers (Caumont-Prim et al. 2013; De Iuliis et al. 2010; Köylü and Faeth 1993; Köylü and Faeth 1994). The reader can refer to the review by Sorensen (2001) on this theory. We shall retain the generalized expression of the Dobbins and Megaridis expression of the scattered signal for a vertical-vertical polarization:

$$SLS_{vv}^{theo}(\theta) \propto N_{agg} \frac{x_p^6}{k^2} F(m) \, \overline{N_p^2 f(\theta)}$$

$$f\left(qR_g, D_f\right) = Aexp\left(-\frac{B}{3}\left(qR_{ga}\right)^2\right) if\left(qR_g\right)^2 < \frac{3C}{2B} \textit{ (Guinier regime)} \qquad [3]$$

$$f\left(qR_g, D_f\right) = A\left(\frac{3C}{2Be}\frac{1}{\left(qR_{ga}\right)^2}\right)^{\frac{C}{2}} if\left(qR_g\right)^2 \geq \frac{3C}{2B} \textit{ (power-law regime)}$$

In Equation 3, N_{agg} is the aggregate number concentration, $x_p = \frac{\pi D_p}{\lambda}$ is the size parameter related to the primary particle size, $k = \frac{2\pi}{\lambda}$ is the wave number, $F(m) = \left|\frac{m^2-1}{m^2+2}\right|^2$ is the scattering function depending on the complex optical index *m* and $\overline{N_p^2 f}$ is an arithmetic mean of the product between the number of primary spheres in the aggregate N_p and the structure factor *f*. The structure factor f reported in Eq. 3 is decomposed into two parts, the Guinier regime that represents the forward diffraction pattern dependent on the aggregate size expressed in terms of the radius of gyration R_{ga}

and the power law regime for larger scattering angles which tends to an asymptotic angular dependence of the form q^{-C}. In classical RDG-FA theory, $A = B = 1$ and $C = D_f$ the fractal dimension of the aggregates, related to the well-known fractal law (Eq. 4, with k_f the fractal prefactor).

$$N_p = k_f\left(R_{ga}/R_p\right)^{D_f} \quad [4]$$

Recent improvements of the RDG-FA theory, from our group (Yon et al. 2014), have shown that multiple scattering effects in the aggregates could lead to $A \neq B \neq 1$ and $C \neq D_f$.

The RDG-FA given in Eq. 3 is dedicated to visible scattering experiments and, for this reason, this theory is focused on the scale of the aggregate size $\left(R_{ga}\right)$. For SAXS experiments, Beaucage (Beaucage 1995) introduced a similar approach to the RDG-FA, considering (Guinier and power-law regimes) for as many scales as necessary for the description of the SAXS measurements. For soot aggregates, the SAXS signal is *a priori* dominated by two length scales related to the aggregate size R_{ga} and to the primary particle gyration radius R_{gp}. Thus, the collected signal can be modeled by the addition of two Guinier-Power law regimes, involving 8 parameters:

$$SAXS^{theo} = \underbrace{G_a \exp\left(-\frac{q^2 R_{ga}^2}{3}\right)}_{S1} + \underbrace{B_a\left(\frac{\left[erf\left(\frac{qR_{ga}}{6^{0.5}}\right)\right]^{3D_f}}{q^{D_f}}\right)\exp\left(-\frac{q^2 R_{gp}^2}{3}\right)}_{S2} + \underbrace{G_p \exp\left(-\frac{q^2 R_{gp}^2}{3}\right)}_{S3} + \underbrace{B_p\left(\frac{\left[erf\left(\frac{qR_{gp}}{6^{0.5}}\right)\right]^{3p}}{q^{p}}\right)}_{S4} \quad [5]$$

The first two terms are related to the aggregates size (the power law is then driven by the fractal dimension D_f) and the two last terms to the primary particle size (fractal dimension is replaced by the Porod exponent *p* related to the surface character of the primary spheres). Note that SAXS presents the advantage over SLS in that it does not depend on the optical index being known due to the fact that m tends toward 1 at very low wavelengths and also multiple scattering effects are negligible.

The prefactor $G_a = N_{agg}(\rho_e V_a)^2 I_e$ is related to the number density of aggregates, to the scattering contrast ρ_e (electron density of the material), to $I_e = r_e^2$ the scattering factor of one electron (the square of the electron radius $r_e = 2.818 \times 10^{-15}\ m$) and V_a the aggregate volume. The same approach remains valid at the scale dominated by the primary spheres. The prefactor $G_p = N_{dp}\left(\rho_e V_p\right)^2 I_e$ is then related to the number density of primary spheres with V_p, the mean volume of the primary spheres. Due to the relations $N_{dp} = \overline{N_p} \times N_{agg}$, $V_a = \overline{N_p} \times V_p$ and because the volume fraction allows the aggregate number density to be related to the mean number of primary spheres per aggregate $\left(f_v = N_{agg}\overline{N_p}\overline{V_p}\right)$, it becomes possible to link the two prefactors G_a and G_b (Eq. 6).

$$\begin{aligned} G_a &= \overline{N_p} \times G_p \\ G_p &= f_v \overline{V_p} \rho_e^2\ I_e \end{aligned} \qquad [6]$$

For spheres, the second prefactor $B_p = 2\pi N_{dp} \rho_e^2 S_p$ is related to the primary spheres surface area and to the primary sphere polydispersity index PDI_p:

$$PDI_p = \frac{B_p R_{gp}^4}{1.62 G_p}\ ;\ PDI_a = \frac{B_a R_{ga}^{D_f}}{G_a} \qquad [7]$$

The polydispersity index is equal to 1 for monodisperse particles and tends toward 5.56 in the case of a lognormal / self-preserving limit. B_a can also be associated to a polydispersity index but, in order to be dimensionless, the gyration radius is raised to the power D_f (Eq. 7). For polymer coil particles with fractal dimension equal to 2, Beaucage (Beaucage 1995) found $PDI_a = 2$. This value will also be considered in this work since the soot fractal dimension is not so far from 2.

By considering lognormal distributions for primary spheres, the corresponding governing parameters (the geometric mean radius $R_{p,geo}$ and the geometric standard deviation $\sigma_{p,geo}$ respectively) are related to R_{gp} and PDI_p by the following relations (Beaucage et al. 2004; Sztucki et al. 2007):

$$R_{p,geo} = R_p \left(\frac{5}{3} exp\left(-14 \ln(\sigma_{p,geo})^2\right)\right)^{1/2} \text{ and } \sigma_{p,geo} = exp\left(\sqrt{\frac{\ln(PDI_p)}{12}}\right) \qquad [8]$$

Additionally, different moments (to order *n*) based on the size distribution of the primary spheres, can be determined by means of the Hatch-Choate equation:

$$\overline{R_p^n} = R_{p,geo}^n exp\left(n^2 \times \frac{\left(ln\left(\sigma_{p,geo}\right)\right)^2}{2}\right) \quad [9]$$

This can be used for example for the determination of the mean volume of the primary spheres: $\overline{V_p} = 4\pi\overline{R_p^3}/3$.

Finally, by combining Equations 4-9, it can been shown that the modeling of the SAXS signal for soot fractal aggregates, can be reduced to the following set of parameters: $\overline{N_p}, D_{p,geo}, \sigma_{p,geo}, f_v, D_f, \rho_e, I_e$ and p. Some of these parameters can be fixed. For example, Fig. 3-B shows that the Porod exponent remains equal to 4, and ρ_e and I_e can be found in the literature. We can also reasonably hypothesize that fractal properties (reported in Table 1) do not change during oxidation, even in case of particle fragmentation (during the aggregation process these parameters also stay constant). Consequently, only $\overline{N_p}, D_{p,geo}, \sigma_{p,geo}\ and f_v$ become necessary for the theoretical evaluation of the SAXS signal. Figure 5 presents such a modeling and extrapolation of the SAXS signal measured at HAB = 2 mm in the oxidizing flame. The different terms appearing in Equation 5 are represented by different colored continuous lines in Fig. 5. It clearly appears that the SAXS measurements made during this campaign, were not sensitive to the aggregate size (this was because of the limited detection range, mentioned in 2.2 above). Only the S3 and S4 terms are really constrained by the experimental data during the model adjustment. This is mainly due to the large size of the miniCAST soot injected at the center of the burner, confirming, by the way, the need for the complementary SLS measurements.

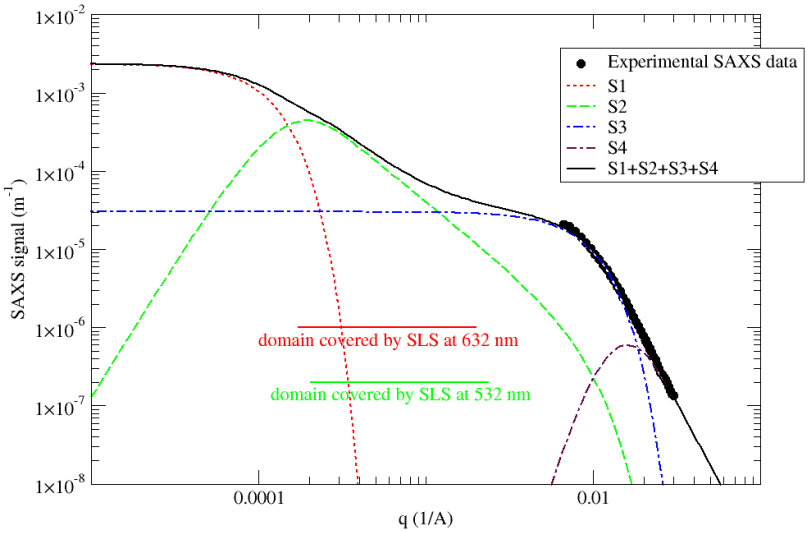

FIG. 5 Example of SAXS theoretical modeling corresponding to the experimental measurement at HAB = 2 *mm* $\overline{N_p} = 75, D_{p,geo} = 26.4\ nm, \sigma_{p,geo} = 1.34, f_v = 20.0\ ppb, \rho_e = 3.59 \times 10^{27}\ m^{-3}, I_e = 7.94 \times 10^{-30} m^2, PDI_a = 2\ , D_f = 1.73, p = 4$).

EXPLOITATION OF THE LII SIGNAL

LII is an optical in-situ technique usually used to determine the soot volume fraction. An intense laser source is used to heat the soot particles leading to a strong emission of radiation. This radiation is collected and interpreted as black body radiation. The intensity of this radiation can be directly linked to the local soot volume fraction (Michelsen et al. 2015):

$$LII \propto f_v \frac{E(m, \lambda_{det})}{{\lambda_{det}}^6} \left(exp\left(\frac{C_2}{\lambda_{det} T_{inc}} \right) - 1 \right)^{-1} \Delta\lambda_{det} \qquad [10]$$

Nevertheless, the LII signal is also strongly dependent on the incandescent soot temperature caused by the laser heating. In the present study, the incandescent temperature of the flame depends on the local initial temperature of the flame (Fig. 2-A) and on the heating produced by the laser beam exposure. This temperature behavior is modeled by solving the following equations inspired by the review (Michelsen et al. 2007):

$$\frac{dM}{dt} = -\frac{\pi D_p^2 W_v \alpha M p_v}{R_p T} \sqrt{\frac{RT}{2W_v}}$$

$$\underbrace{\rho\, C_p \frac{\pi}{6} D_p^3(t) \frac{dT}{dt}}_{heating} = \underbrace{\frac{\pi^2 D_p^3 E(m)}{\lambda_{laser}} F(t)}_{absorption} - \underbrace{\frac{2\, K_a \pi D_p^2}{D_p(t) + G\ lpm} (T - T0)}_{conduction} - \underbrace{\frac{199\pi^3\, D_p^3(t) k_b^5 E(m)}{h(hc)^3} (T^5 - T_0^5)}_{Radiation} + \underbrace{\frac{\Delta H_v}{W_s} \frac{dM}{dt}}_{Sublimation} \qquad [11]$$

This system of differential equations can be solved for different heights above the burner by considering the local flame temperature (Fig. 2-A) and the local primary particle size diameter as initial conditions. The temporal behavior of the particle temperature so obtained, is then used to determine the LII signal by using Eq. 10. Fig. 6 presents some results of this modeling for three heights above the burner. It can be seen that the diameter of the primary spheres does not vary significantly during the laser pulse (the sublimation process is not significant). On the other hand, the temperature profile and consequently the LII temporal decay are strongly dependent on the HAB due to the strong variation of the flame temperature. The modeled maximum of the LII signal is seen to appear earlier with increasing HAB. The same decay is seen in the experimental LII data (not presented).

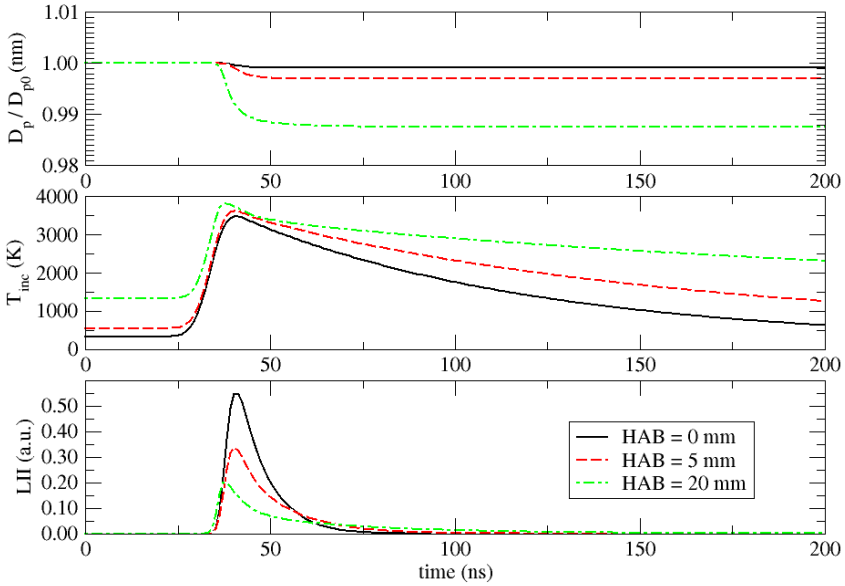

FIG. 6 Modeling of the temporal relative evolution of the primary sphere diameter, soot incandescence temperature and LII signal after laser pulse for soot injected in the flame at different heights above the burner.

With this method, the local volume fraction is fitted in order to match the modeled maximum LII signal with the measured signal. Note that the volume fraction at HAB = 0 mm is set to 27.2 ppb in accordance with PPS measurements on cold soot (Table 1). FIG. 4 shows the volume fraction profile obtained by applying this procedure, in red dots. The continuous red line is determined by a fitting process according to the function:

$f_v = \frac{c}{z+d}$ with $c = 0.134\ m.ppb$, $d = 4.735 \times 10^{-3}\ m$, z the HAB expressed in m. [12]

This figure shows that not taking into account, the local temperature and primary particle size, *i.e.* considering that the maximum of the LII signal is directly proportional to the volume fraction, tends to overestimate the local volume fraction.

ANALYSIS BASED ON THE COUPLING OF SLS/SAXS AND LII MEASUREMENTS

As shown in the previous sections, the SAXS fitting with the Beaucage model implies seeking $\overline{N_p}, D_{p,geo}, \sigma_{p,geo}$ and f_v. We observed that the q-domain covered by SAXS is particularly suited for the determination of the primary particle size distribution parameters ($D_{p,geo}, \sigma_{p,geo}$). On the other hand, for the current experiment and for the chosen target to detector distance used on the SWING beamline, the aggregate size could not be addressed (Fig. 5). Nevertheless, the size of the aggregates, here represented by the $\overline{N_p}$ parameter, is of prime interest for the modeling of the SLS signal. Indeed, from Eq. 3, it can easily be shown that the ratio between SLS signal and the volume fraction, depends directly on the aggregate size distribution:

$$\frac{SLS_{vv}^{theo}}{f_v} = \alpha\, F(m) \frac{\overline{D_p^6}}{\overline{D_p^3}} \frac{\overline{N_p^2 f(\theta)}}{\overline{N_p}} \quad [13]$$

The moments based on the primary particle size distribution are determined using Hatch-Choate equation (Eq. 9) and those based on the number of primary spheres per aggregate are numerically computed, based on the assumption of lognormal size distributions for the gyration diameter ($D_{a,geo}, \sigma_{a,geo}$) and structure factor reported in Eq. 3. Note that the fractal parameters and optical constants are considered to stay constant during the oxidation process as well as the geometric standard deviation of the aggregate size distribution based on the gyration diameter ($\sigma_{a,geo} = 1.9$, see Table 1).

In addition, we have shown that LII is sensitive to the volume fraction f_v. Consequently, the proposed inversion process is to constrain the SAXS data fitting with the LII and SLS data. Indeed, for each HAB, the volume fraction is fixed by the LII measurement and $\overline{N_p}, D_{p,geo}, \sigma_{p,geo}$ are sought using a least-square method in order to fit together the SAXS (Eq. 5) and SLS (Eq. 13) results. Since this

procedure is not conventional, the Igor Pro based "IRENA" package (Ilavsky 2006), often employed in the literature, was not used in the present study. Instead, the fitting procedure has been coded in Scilab with the use of the Levenberg–Marquardt least-squares algorithm. Note that, because the volume fraction determination is dependent of the primary sphere diameter (see section above), an iteration procedure was used to converge (Fig. 7).

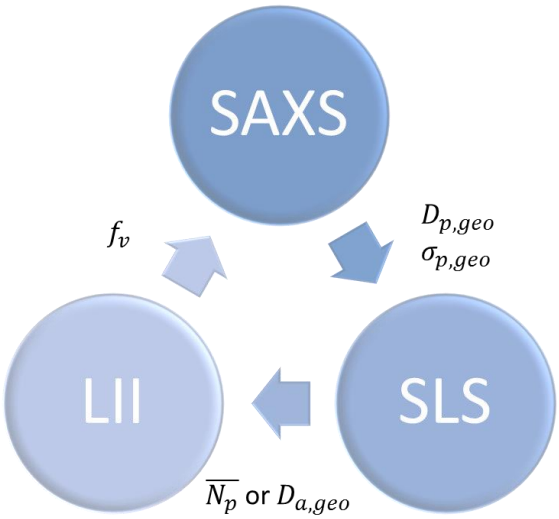

FIG. 7 Representation of the iteration procedure used for the determination of the parameters.

The unknown constant of proportionality α, related to the scattering measurement in Eq. 13, is determined in order that the inversion process yields $D_{a,geo} = 222\ nm$ at HAB = 2 mm, based on the hypothesis of continuity of the aggregate size once injected into the oxidizing flame (value reported in Table 1 for the size distribution measured by SMPS, expressed as the gyration diameter).

INTERPRETATION OF THE RESULTS

By applying the previously described inversion process, the SAXS, SLS and LII measurements have allowed the aggregate size $\overline{N_p}$, the primary particle modal diameter $D_{p,geo}$, the geometrical standard deviation $\sigma_{p,geo}$ and the volume fraction f_v (already presented in Fig. 4) to be determined. By using relations expressed in section 4.1, it is then possible to determine the aggregate and the primary sphere number densities (respectively N_{agg} and N_{dp}). Figure 5 is an example of the application of this fitting procedure for HAB = 2 mm. A first notable result is that the fitting procedure is very good except for HAB = 10 and 24 mm (see the Pearson's correlation coefficient represented by red crosses in Fig. 8).

This indicates that volume fractions profiles derived from the LII measurements, are in very good agreement with SAXS data. Indeed, we have previously shown (see equation 6) that the amplitude of the SAXS signal (G_a and G_p terms) are directly proportional to f_v. Nevertheless, for this to be possible, the electron density had to be fixed to $\rho_e = 3.59 \times 10^{27}\ m^{-3}$ *i.e.* 190 times lower than value found in the literature for graphite (McDonald 2013). This difference of magnitude cannot be explained by an uncertainty concerning the estimation of the volume fraction of soot produced by the miniCAST. Indeed, in order to have a good accordance between LII and SAXS signal by keeping the electron density of graphite cited above, f_v should have been determined with a factor 36100 (=190^2) lower than value determined with PPS/TEOM method. Indeed, it is worth noting that the currently determined electron density is only 8 times lower than the total electron density deduced by fitting soot extinction spectra with Drude-Lorentz dispersion model for the same operating conditions of the miniCAST (Bescond et al. 2016).

The results of the inversion process are reported in Fig. 8. In this figure, black filled boxes correspond to the evaluation of the parameters on cold soot by non-optical techniques (value reported or deduced from Tab. 1). For example, $D_{p,geo}$ and $\sigma_{p,geo}$ determined by the inversion process at HAB = 2 mm are found to be in excellent agreement with the value determined by the automatized analysis of the MET images (EDM-SBS analysis (Bescond et al. 2014)). This is a performance indicator of the Beaucage model for polydisperse spheres (Eq. 5 and Eq. 7). Except for 2 HAB for which fitting is less good, it clearly appears that modal diameter of primary particles decreases with the oxidation process and that geometric standard deviation increases.

As discussed before, the aggregate size determination is principally governed by SLS measured at 33° scattering angle and by LII measurement (Eq. 13). It must be noted that such an inversion is only possible when considering the multiple scattering corrections in Eq. 3. Indeed, at this scattering angle, for $\lambda = 532\ nm$, the theoretical ratio $\overline{N_p^2 f(\theta)}/\overline{N_p}$ from classical RDG-FA theory rapidly tends to a constant for large aggregates. Fortunately, the taking into account of multiple scattering effects in RDG-FA theory (that depends on the number of primary spheres and also on the primary particle size)

enables the variation with HAB of the ratio of the SLS signal and the volume fraction to be interpreted. By considering such corrections, one can observe an unexpected rapid increase in aggregate size up to HAB = 10 mm. It seems that the decrease of the primary particle mass due to the oxidation process and the rapid increase of the temperature of the particles, causes significant re-aggregation once the soot is injected into the flame. Nevertheless, for larger HABs, the aggregate size begins to decrease indicating the beginning of the fragmentation process. This suggests that fragmentation occurs when the primary sphere diameters are reduced by approximately 20%. It is interesting to note that the magnitude is in good agreement with the overlapping primary sphere particles reported in previous studies (Brasil et al. 1999; Ouf et al. 2010; Thomas et al. 2014). Indeed, by keeping the primary spheres center-to-center distance constant for two adjacent monomers and by decreasing their diameter, the contact between them is broken when the relative decrease of the diameters corresponds to the initial projected overlapping coefficient (approximatively 29% for miniCAST (Thomas et al. 2014)). By considering this evaluation of the aggregate size and other results, it becomes possible to evaluate the aggregate number density. This parameter first decreases due to the re-aggregation process and perhaps to the total oxidation of smaller particles. When the inverse of that density is plotted as a function of residence time (not presented), it appears that the re-aggregation process takes the form $N_{agg}^{-1}(t) = 9.17 \times 10^{-11} t^{1.25}$ for t expressed in seconds and N_{agg}^{-1} in m^3. This nonlinear dependence on residence time reveals a kinetic exponent $z = 1.25$ which is typical of fractal aggregation in the intermediate continuum regime (Pierce et al. 2006). Nevertheless, the rate at which aggregate size increases during this stage, appears to be very high compared to the conventional rates encountered in the literature. Whatever, the increase of the aggregate density occurring for HAB ≥ 18 mm, probably due to the fragmentation process, is in good agreement with previous observations by Neoh et al. (1985) and Ghiassi et al. (2016).

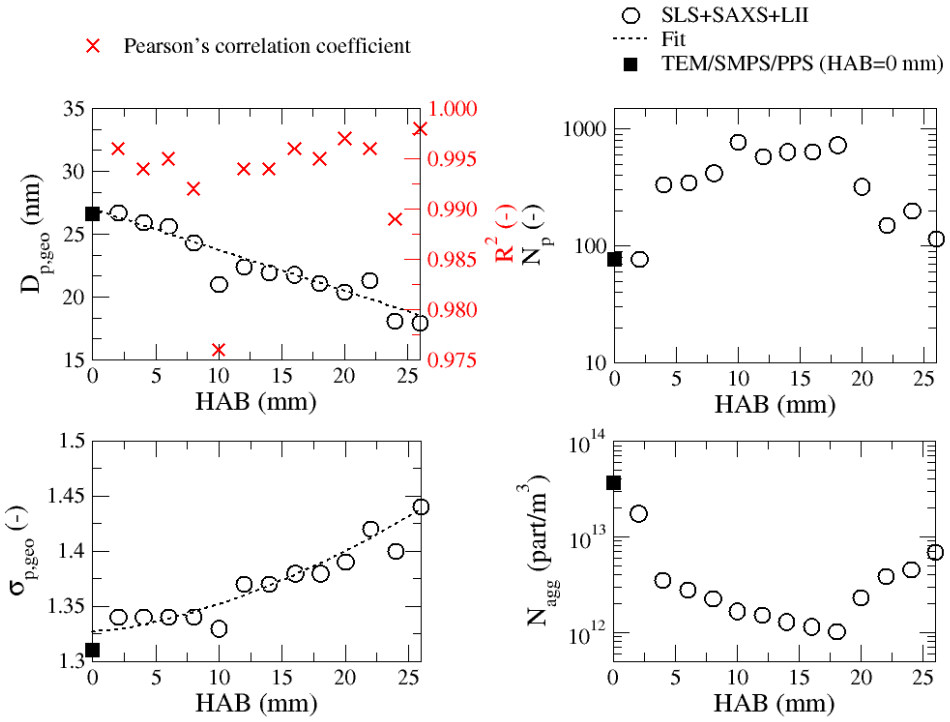

FIG. 8 Result of the SLS/SAXS/LII data inversion. Reported values at HAB = 0 mm correspond to the values determined on fresh soot by non-optical methods (MET/SMPS/PPS-TEOM).

The observed decrease of the modal primary diameter has already been observed by TEM analysis (Puri et al. 1994) but, to our knowledge, a quantitative description of the geometric standard deviation has never been performed before. Both the modal diameter decreases and the geometric standard deviation increases as a function of the HAB, reported in Fig. 8, can successfully be modeled. Indeed, by considering the distribution of the injected soot as a starting point, we can show that the lognormal distribution of the primary spheres, measured at any HAB, can be modeled with the equation reported in Eq. 14.

$$\frac{d\widetilde{D_p}}{dt} = -\frac{1}{\tau}\widetilde{D_p}^{n} \Leftrightarrow \frac{d\widetilde{V_p}}{dt} = -\frac{3}{\tau}\widetilde{D_p}^{n+2}$$

$$\text{with } \widetilde{D_p} = \frac{D_p}{D_{p,geo}(HAB=0)} \text{ and } \widetilde{V_p} = \frac{V_p}{V_{p,geo}(HAB=0)} \qquad [14]$$

This is illustrated in the left part of FIG. 9 for two HABs (14 mm and 26 mm respectively). It is clearly observed that the lognormal shape is well conserved by applying this model. The right-hand part of Fig. 9 presents the parameters n and τ adapted to best fit the model (Eq. 14) on the SAXS data

interpretation (Fig. 8) for each HAB. The power indice *n* is shown to decrease with HAB but it seems to remain between 0 and 1. According to Eq. 14 expressed in terms of primary sphere volume, it appears that the primary sphere volume or mass rate reduction is proportional to D_p to the power of $n+2$ with $2 < n+2 < 3$. This suggests that the oxidation process is not limited to a pure surface reaction but seems to be reactive with a shell of the primary spheres in accordance with observations by (Ishiguro et al. 1991) "*the disintegration of soot particles occurring in the late stage of oxidation is not due to the dissociation of carbon atoms at the edges of layer planes but is due rather to the stripping of small crystallites existing on the outer surface of the soot particles*". The greater the residence time, the more *n* decreases indicating that the thickness of the reacting shell decreases, *i.e*. the oxidation regime is transient from regime 2 to regime 3 based on the definition reported by Stanmore et al. (2001). This accompanies the increase of the flame temperature. $n \neq 1$ is directly responsible for the change of the geometrical standard deviation. On the other hand, the parameter τ is an indicator of the rate at which the primary particle diameter decreases during the oxidation process. It is shown in Fig. 9, that the characteristic time τ also decreases with HAB. This can be consistent with the fact that the accessible oxidizing material decreases (thickness of the shell related to n) and also that oxidizing species concentrations may reducing with HAB (see for example (Neoh et al. 1981)).

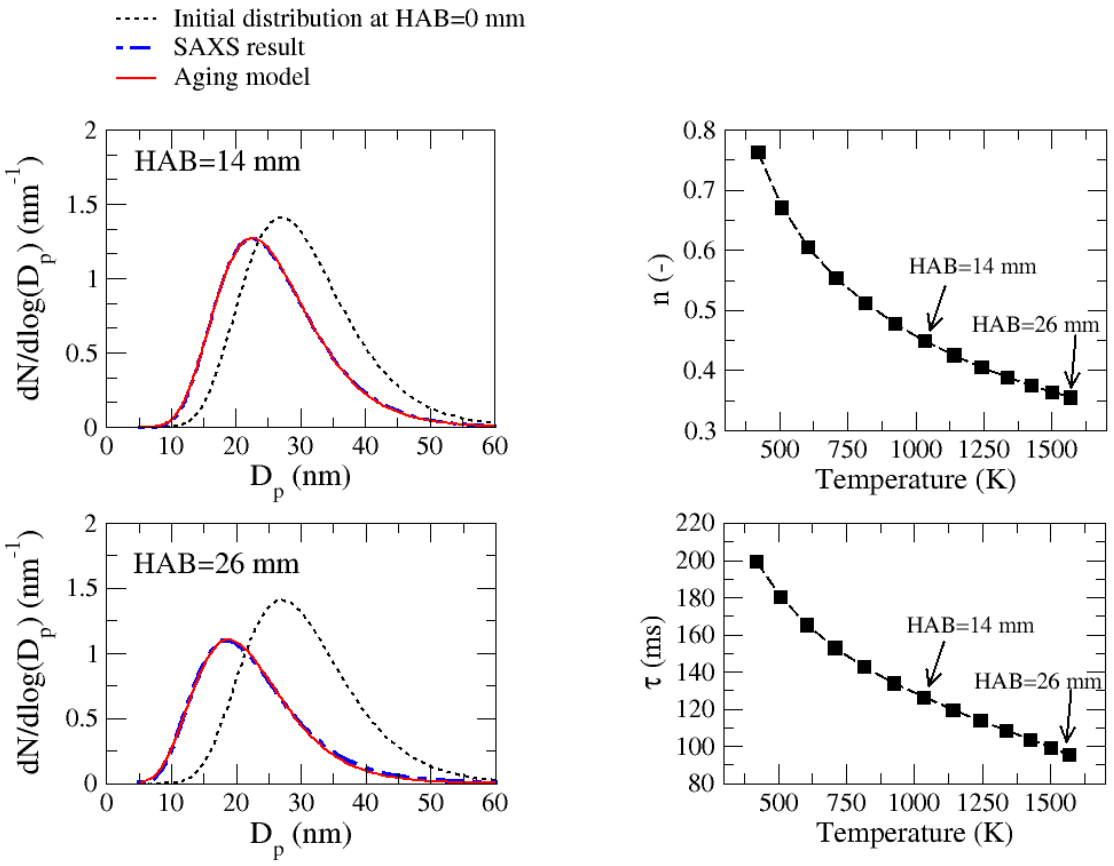

FIG. 9 Application of the model $\frac{d\widetilde{D_p}}{dt} = -\frac{1}{\tau}\widetilde{D_p}^{n}$ for the description of the primary sphere modal diameter and geometric standard deviation behavior along the flame.

Figure 10-A represents in red, the mass concentration $C_s = \rho_p f_v$ deduced from the corrected LII measurement and by considering the bulk density reported in Table 1 as a function of the residence time. For this calculation, the bulk density ρ_p is considered to be constant suggesting that the desorption of volatile organic components and internal graphitization due to the high temperatures, is reduced. This is a reasonable assumption for the present combustion conditions of the miniCAST since as soon as injected into the flame, the particles considered present a very low content of organic materials (Table 1) and a relatively ordered microstructure (Bescond et al. 2016).

In consequence, providing a constant coefficient mass based reaction rate k_m, the observed exponential decrease of the mass concentration in Fig. 10-A could be interpreted as a natural solution of the pseudo-first-order rate equation (Eq. 15), often considered for the evaluation of the mass reduction during the oxidation process.

$$\frac{dC_s}{dt} = -k_m C_s \qquad [15]$$

Nevertheless, the thermal dilution occurring in the flame may also be responsible for a decrease of the determined mass concentration, without invoking any oxidation. Fortunately, this thermal dilution can be determined thanks to the flame velocity measurements reported in Fig. 2-B (see appendix for explanation of the method). By considering this effect, the so determined k_m coefficient is shown to strongly decrease with residence time (continuous blue curve in Fig. 10-A). The obtained order of magnitude of reaction rate is found to be larger than ones determined by (Ma et al. 2013) based on DMA-APM measurements on soot sampled in an Santoro ethylene diffusion burner. The observed decrease suggests that oxidation efficiency decreases with HAB even if local temperature increases. This may be explained by the reduction of oxidizing species (mainly O_2 and OH) that comes along with the increasing distance from the front of flame. This result is in agreement with the previously commented decrease of parameters *n* and τ in FIG. 9.

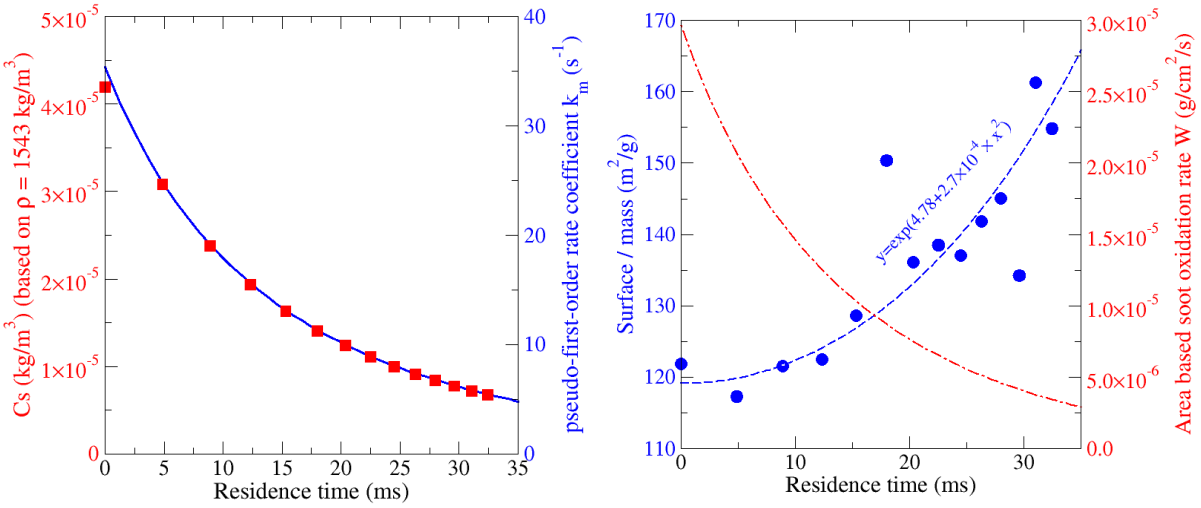

A: Mass concentration deduced from LII measurement (red plain boxes) and determined pseudo-first-order rate of the oxidation process based on mass (blue plain curve).

B: Aggregate surface – mass ratio (plain blue circles) and the area based soot oxidation rate (red dash curve).

FIG. 10 Time evolution of the mass concentration and of the ratio surface/mass of the particles.

Figure 10-B also reports the ratio between the aggregate surface and the mass (in blue plain circles). The observed increase is directly caused by the primary particle size reduction. It is very interesting to compare this results with BET measurements performed by Ishiguro et al. (1991), for Diesel soot, during oxidation with air in a furnace held at 500 °C. Indeed, these authors observed an increase in the nitrogen determined surface area from 52 to 296 m^2/g, as well as Otto et al. (1980), in very good agreement with the present observations but limited to a lower degree of oxidation. But, in the study by Ishiguro et al. (1991), the BET results were not perfectly corroborated by MET analysis, invoking a change of the aggregate porosity during the oxidation process. In the present study, the surface area increase is determined by a precise determination of the primary particle size reduction by means of the SAXS technique, with the hypothesis of sharp spheres (Porod exponent remaining equal to 4) without invoking any possible change of the internal porosity during the oxidation process. Once again, this can be specifically due to the use of soot particles presenting, once injected in the flame, a low carbon organic fraction and a relatively ordered microstructure. Indeed, recent investigation by *in-situ* Raman micro-spectroscopy (Ess et al. 2016), has demonstrated that the microstructure of these miniCAST's soot particles is little modified under a long-time oxidation process (limited to 600 °C). Furthermore, it has also been demonstrated in a previous study (Ess et al. 2016), that the microstructures of soot particles indicating significantly different initial composition, tend to the microstructure of our present soot samples at the end of their desorption / oxidation process.

Based on the assumption that oxidation is a surface based mechanism, Neoh et al. (1981) and also Echavarria et al. (2011) preferred, in respect to the first order law (Eq. 15), to introduce another parameter called specific soot burnout rate W:

$$\frac{dC_s}{dt} = -WA \qquad [16]$$

With A, representing the soot available surface area (m^2/m^3). In fact, it can be shown that W is simply obtained by dividing k_m (reported in Fig. 10-A) by the specific surface (surface – mass ratio fit reported in Fig. 10-B). The so determined specific soot burnout rate is reported in red in Fig. 10-B. The order of magnitude of this parameter is found to be 100 times lower than values reported by Garo

et al. (1990) who considered spherical particles in their optical measurements analysis. On the other hand, the reported results in this study are in accordance with the one determined by (Higgins et al. 2002) using a tandem DMA and by (Echavarria et al. 2011) based on SMPS measurements (also considering soot as spherical particles). But, contrarily to the results reported in that last paper, in the present study, this parameter is found to decrease with HAB, in coherence with the decrease of oxidizing species in the surrounding gas and the decrease of the reactive shell thickness on the primary sphere surface as described before.

CONCLUSION

In-situ analysis of an in-flame soot oxidation process was performed by coupling three optical techniques namely SAXS (x-ray scattering), SLS (visible light scattering) and LII (laser induced incandescence). The complementarity of these techniques allowed the soot volume fraction, the aggregate size, the aggregate density and the primary sphere size distribution to be determined. Nevertheless, many cautions are needed to satisfactorily couple these techniques, such as taking into account the local temperature change along the flame for the interpretation of the LII as well as of multiple scattering for the SLS results. In order only to observe the oxidation process, soot produced by a miniCAST generator and characterized by non-optical techniques (TEM/PPS/TEOM/SMPS) were injected into a non-sooting flame. The results confirmed that the mass loss rate is well described by a first order rate equation and that the in-flame dynamics of oxidation is in good agreement with other results performed *ex-situ* in furnaces and interpreted using Arrhenius equations. A strong agglomeration process is detected at lower heights above the burner certainly due to the increase of the particle mobility caused by the reduction in mass of the particles and the increase of the local temperature. This phenomenon is followed by a breakup of the soot aggregates when the sizes of the primary particles are reduced by a factor of 20% corresponding to the initial degree of primary spheres overlapping. This study also allowed the evolution of the primary particle size distribution to be determined. It was shown that the decrease of the modal diameter was accompanied by a significant increase in the geometric standard deviation. A model has been proposed to mimic this behavior suggesting that the oxidation process acts on a shell surrounding the primary sphere, whose thickness

decreases during the oxidation process resulting in a decrease of the oxidation efficiency. This decrease must be explained by a decrease of the oxidizing components at vicinity of soot with increasing the height above the burner, even if local temperature increases. This decrease of oxidation efficiency is confirmed by the observed decrease of the first order reaction mass rate and of the specific soot burnout rate that are shown to decrease with the height above the burner. Finally, it was shown that the surface area increases during oxidation due to the monomer diameter decrease without invoking any change of the soot microstructure. One prospective of this work is to apply the same coupling of techniques with injection into non-sooting flames of different temperatures and of soot presenting other initial compositions and microstructures. The effect of additives (ferrocene, halogens, urea, etc.) on the oxidation of soot particles is another main prospect of the present study. A determination of the surrounding oxidizing species concentrations would be helpful for the exploitation of these results for kinetic models.

ACKNOWLEDGMENTS

This work was conducted within the framework of French Carnot Institute Energy and Propulsion Systems (ESP, project Dimosoot). We acknowledge SOLEIL for provision of synchrotron radiation facilities.

REFERENCES

Beaucage, G. (1995). Approximations leading to a unified exponential/power-law approach to small-angle scattering. *J.of Appl. Cryst.*, 28:717-728.

Beaucage, G., Kammler, H., Pratsinis, S. (2004). Particle size distributions from small-angle scattering using global scattering functions. *J.of Appl. Cryst.*, 37:523-535.

Bescond, A., Yon, J., Ouf, F.-X., Ferry, D., Delhaye, D., Gaffié, D., Coppalle, A., Rozé, C. (2014). Automated Determination of Aggregate Primary Particle Size Distribution by TEM Image Analysis: Application to Soot. *Aerosol Sci. Tech.*, 48:831-841.

Bescond, A., Yon, J., Ouf, F.X., Rozé, C., Coppalle, A., Parent, P., Ferry, D., Laffon, C. (2016). Soot optical properties determined by analyzing extinction spectra in the visible near-UV: Toward an optical speciation according to constituents and structure. *J. Aerosol Sci.*, 101:118-132.

Bradley, D., Matthews, K. (1968). Measurement of high gas temperatures with fine wire thermocouples. *J. Mech. Eng. Sci.*, 10:299-305.

Brasil, A.M., Farias, T.L., Carvalho, M.G. (1999). A recipe for image characterization of fractal-like aggregates. *J. Aerosol Sci.*, 30:1379.
Caumont-Prim, C., Yon, J., Coppalle, A., Ouf, F.-X., Fang Ren, K. (2013). Measurement of aggregates' size distribution by angular light scattering. *J. Quant. Spectrosc. Radiat. Transfer*, 126:140-149.
De Iuliis, S., Maffi, S., Cignoli, F., Zizak, G. (2010). Three-angle scattering/extinction versus TEM measurements on soot in premixed ethylene/air flame. *Appl. Phys. B-Lasers O*, 102:891-903.
Di Stasio, S., LeGarrec, J.-L., Mitchell, J. (2011). Synchrotron radiation studies of additives in combustion, II: soot agglomerate microstructure change by alkali and alkaline-earth metal addition to a partially premixed flame. *Energy & Fuels*, 25:916-925.
di Stasio, S., Mitchell, J., Legarrec, J., Biennier, L., Wulff, M. (2006). Synchrotron SAXS <in situ> identification of three different size modes for soot nanoparticles in a diffusion flame. *Carbon*, 44:1267-1279.
Dobbins, R.A., Megaridis, C.M. (1991). Absorption and scattering of light by polydisperse aggregates. *Appl. Opt.*, 30:4747-4754.
Echavarria, C.A., Jaramillo, I.C., Sarofim, A.F., Lighty, J.S. (2011). Studies of soot oxidation and fragmentation in a two-stage burner under fuel-lean and fuel-rich conditions. *P. Combust. Inst.*, 33:659-666.
Ess, M., Ferry, D., Kireeva, E., Niessner, R., Ouf, F.-X., Ivleva, N. (2016). In situ Raman microspectroscopic analysis of soot samples with different organic carbon content: Structural changes during heating. *Carbon*, 105:572-585.
Förster, G.D., Girault, M., Menneveux, J., Lavisse, L., Jouvard, J.-M., de Lucas, M.d.C.M., Potin, V., Ouf, F.-X., Kerkar, M., Le Garrec, J.-L. (2015). Oxidation-Induced Surface Roughening of Aluminum Nanoparticles Formed in an Ablation Plume. *Phys. Rev. Lett.*, 115:246101.
Garo, A., Lahaye, J., Prado, G. (1988). Mechanisms of formation and destruction of soot particles in a laminar methane-air diffusion flame. *Symposium (International) on Combustion*, 21:1023-1031.
Garo, A., Prado, G., Lahaye, J. (1990). Chemical aspects of soot particles oxidation in a laminar methane-air diffusion flame. *Combust. Flame*, 79:226-233.
Ghiassi, H., Jaramillo, I.C., Toth, P., Lighty, J.S. (2016). Soot oxidation-induced fragmentation: Part 2: Experimental investigation of the mechanism of fragmentation. *Combust. Flame*, 163:170-178.
Higgins, K.J., Jung, H., Kittelson, D.B., Roberts, J.T., Zachariah, M.R. (2002). Size-Selected Nanoparticle Chemistry: Kinetics of Soot Oxidation. *J. Phys. Chem. A*, 106:96-103.
Ilavsky, J. (2006). Irena 2 package of SAS data evaluation and modeling macros for Igor Pro.
Ishiguro, T., Suzuki, N., Fujitani, Y., Morimoto, H. (1991). Microstructural changes of diesel soot during oxidation. *Combust. Flame*, 85:1-6.
Ishiguro, T., Yakatori, Y., Akihama, K. (1997). Microstructure of diesel soot particles probed by electron microscopy: first observation of inner core and outer shell. *Combust. Flame*, 108:231.
Jung, H., Kittelson, D.B., Zachariah, M.R. (2004). Kinetics and visualization of soot oxidation using transmission electron microscopy. *Combust. Flame*, 136:445-456.
Kim, S., Fletcher, R., Zachariah, M. (2005). Understanding the difference in oxidative properties between flame and diesel soot nanoparticles: The role of metals. *Env. Sc. and Tech.*, 39:4021-4026.
Kong, W., Liu, F. (2009). Numerical study of the effects of gravity on soot formation in laminar coflow methane/air diffusion flames under different air stream velocities. *Combust. Theor. Model.*, 13:993-1023.
Köylü, U., Faeth, G. (1993). Radiative properties of flame-generated soot. *J. Heat Trans.-T ASME* 115.
Köylü, Ü.Ö., Faeth, G.M. (1994). Optical properties of overfire soot in buoyant turbulent diffusion flames at long residence times. *J. Heat Transf.*, 116:152-159.
Lee, K.B., Thring, M.W., Beér, J.M. (1962). On the rate of combustion of soot in a laminar soot flame. *Combust. Flame*, 6:137-145.

Lighty, J., Sarofim, A., Echavarria, C., Jaramillo, I., Levinthal, J., Romano, V. (2011). Effects of Soot Structure on Soot Oxidation Kinetics, SERDP ed. Department of chemical Engineering University of Utah.
Lyons, V.J., Gracia-Salcedo, C.M. (1989). Determination of combustion gas temperatures by infrared radiometry in sooting and nonsooting flames. DTIC Document.
Ma, X., Zangmeister, C., Zachariah, M. (2013). Soot oxidation kinetics: a comparison study of two tandem ion-mobility methods. *J. Phys. Chem. C*, 117:10723-10729.
McDonald, M.J. (2013). SMALL-ANGLE X-RAY SCATTERING STUDIES OF NANOSTRUCTURED RESPIRATOR AND BATTERY MATERIALS.
Michelsen, H., Liu, F., Kock, B.F., Bladh, H., Boïarciuc, A., Charwath, M., Dreier, T., Hadef, R., Hofmann, M., Reimann, J. (2007). Modeling laser-induced incandescence of soot: a summary and comparison of LII models. *Appl. Phys. B-Lasers O*, 87:503-521.
Michelsen, H., Schulz, C., Smallwood, G., Will, S. (2015). Laser-induced incandescence: Particulate diagnostics for combustion, atmospheric, and industrial applications. *Prog. Energ. Combust.*
Mitchell, J., LeGarrec, J.-L., Saidani, G., Lefeuvre, F., Di Stasio, S. (2013). Synchrotron Radiation Studies of Additives in Combustion, III: Ferrocene. *Energy & Fuels*, 27:4891-4898.
Mitchell, J., Legarrec, J., Florescumitchell, A., Distasio, S. (2006). Small-angle neutron scattering study of soot particles in an ethylene–air diffusion flame. *Combust. Flame*, 145:80-87.
Moore, R.H., Ziemba, L.D., Dutcher, D., Beyersdorf, A.J., Chan, K., Crumeyrolle, S., Raymond, T.M., Thornhill, K.L., Winstead, E.L., Anderson, B.E. (2014). Mapping the Operation of the Miniature Combustion Aerosol Standard (Mini-CAST) Soot Generator. *Aerosol Sci. Tech.*, 48:467-479.
Mueller, M.E., Blanquart, G., Pitsch, H. (2011). Modeling the oxidation-induced fragmentation of soot aggregates in laminar flames. *P. Combust. Inst.*, 33:667-674.
Neoh, K.G., Howard, J.B., Sarofim, A.F. (1981). Soot Oxidation in Flames, in: Siegla, D.C., Smith, G.W. (Eds.), Particulate Carbon: Formation During Combustion. Springer US, Boston, MA, pp. 261-282.
Neoh, K.G., Howard, J.B., Sarofim, A.F. (1985). Twentieth Symposium (International) on CombustionEffect of oxidation on the physical structure of soot. *Symposium (International) on Combustion*, 20:951-957.
Ossler, F., Vallenhag, L., Canton, S.E., Mitchell, J.B.A., Le Garrec, J.-L., Sztucki, M., di Stasio, S. (2013). Dynamics of incipient carbon particle formation in a stabilized ethylene flame by in situ extended-small-angle- and wide-angle X-ray scattering. *Carbon*, 51:1-19.
Otto, K., Sieg, M.H., Zinbo, M., Bartosiewicz, L. (1980). The Oxidation of Soot Deposits from Diesel Engines. SAE International.
Ouf, F.-X., Yon, J., Ausset, P., Coppalle, A., Maillé, M. (2010). Influence of Sampling and Storage Protocol on Fractal Morphology of Soot Studied by Transmission Electron Microscopy. *Aerosol Sci. Tech.*, 44:1005 - 1017.
Pierce, F., Sorensen, C., Chakrabarti, A. (2006). Computer simulation of diffusion-limited cluster-cluster aggregation with an Epstein drag force. *Phys. Rev. E*, 74.
Puri, R., Santoro, R.J., Smyth, K.C. (1994). The oxidation of soot and carbon monoxide in hydrocarbon diffusion flames. *Combust. Flame*, 97:125-144.
Schmid, J., Grob, B., Niessner, R., Ivleva, N.P. (2011). Multiwavelength Raman microspectroscopy for rapid prediction of soot oxidation reactivity. *Anal. Chem.*, 83:1173-1179.
Seitzman, J., Wainner, R., Yang, P. (1999). Soot-velocity measurements by particle vaporization velocimetry. *Opt. Lett.*, 24:1632-1634.
Seong, H.J., Boehman, A.L. (2012). Studies of soot oxidative reactivity using a diffusion flame burner. *Combust. Flame*, 159:1864-1875.
Sirignano, M., Ghiassi, H., D'Anna, A., Lighty, J.S. (2016). Temperature and oxygen effects on oxidation-induced fragmentation of soot particles. *Combust. Flame*, 171:15-26.
Sorensen, C. (2001). Light scattering by fractal aggregates: a review. *Aerosol Sci. Tech.*, 35:648-687.
Sorensen, C.M. (2013). Q-space analysis of scattering by particles: A review. *J. Quant. Spectrosc. Radiat. Transfer*.

Stanmore, B.R., Brilhac, J.F., Gilot, P. (2001). The oxidation of soot: a review of experiments, mechanisms and models. *Carbon*, 39:2247-2268.
Sztucki, M., Narayanan, T., Beaucage, G. (2007). In situ study of aggregation of soot particles in an acetylene flame by small-angle x-ray scattering. *J. of Appl. Phy.*, 101:114304-114304-114307.
Thomas, D., Ouf, F., Gensdarmes, F., Bourrous, S., Bouilloux, L. (2014). Pressure drop model for nanostructured deposits. *Sep. Purif. Technol.*, 138:144-152.
Xu, F., El-Leathy, A., Kim, C., Faeth, G. (2003). Soot surface oxidation in hydrocarbon/air diffusion flames at atmospheric pressure. *Combust. Flame*, 132:43-57.
Xu, F., Sunderland, P.B., Faeth, G.M. (1997). Soot formation in laminar premixed ethylene/air flames at atmospheric pressure. *Combust. Flame*, 108:471-493.
Yon, J., Bescond, A., Ouf, F.X. (2015). A simple semi-empirical model for effective density measurements of fractal aggregates. *J. Aerosol Sci.*, 87:28-37.
Yon, J., Liu, F., Bescond, A., Caumont-Prim, C., Rozé, C., Ouf, F.X., Coppalle, A. (2014). Effects of multiple scattering on radiative properties of soot fractal aggregates. *J. Quant. Spectrosc. Radiat. Transfer*, 133:374-381.